Journal of
Materials Chemistry C

Accepted Manuscript

This article can be cited before page numbers have been issued, to do this please use: A. A. Godoy, G. Gómez, A. M. M. Kaczmarek, R. Van Deun, O. J. Furlong, F. Gándara, A. Monge, M. C. Bernini and G. Narda, *J. Mater. Chem. C*, 2017, DOI: 10.1039/C7TC04006G.

ROYAL SOCIETY OF CHEMISTRY

rsc.li/materials-c

View Article Online
DOI: 10.1039/C7TC04006G

Journal Name

ARTICLE

Sensing properties, energy transfer mechanism and tuneable particle size processing of luminescent two-dimensional rare earth coordination networks

Received 00th January 20xx,
Accepted 00th January 20xx

DOI: 10.1039/x0xx00000x

www.rsc.org/

Agustín A. Godoy[a], Germán E. Gomez[a], Anna M. Kaczmarek[b], Rik Van Deun[b], Octavio J. Furlong[c], Felipe Gándara[d], María A. Monge[d], María C. Bernini[a,*] and Griselda E. Narda[a]

A new isostructural family of layered coordination networks (CNs) based on rare earth elements and mixed ligands, was hydrothermally synthesized and fully characterized. The set of compounds with a general formula [REE(Salicylate)(Succinate)$_{0.5}$(H_2O)] (with REE = Ho or Y) belongs to the monoclinic $P2_1/c$ space group. Top-down methods were implemented in order to obtain nano-sized CN particles for potential applications in thin films fabrication. The solid state photoluminescence (SSPL) of the Eu, Tb and Eu/Tb doped samples was explored in terms of excitation/emission spectra, lifetime values and quantification of light emission by the CIE chromaticites calculation. Measurement of the triplet state energy of the ligand at low temperature was carried out by analysing the SSPL of the Y-based compound; energy transfer pathways are analysed. According to the high performance as green emitter of the Tb-doped compound, thermal and chemical sensing assays were carried out.

1. Introduction

The field of Metal Organic Frameworks (MOFs), or in a more general sense, Coordination Networks (CNs)[1,2], has experienced a great progress in the last decade, not only by the design and synthesis of specific crystal structures, but also by the capability of controlling particle size and shape. In terms of salient structures that make possible outstanding behaviours, there are different kinds of materials: those exhibiting flexibility[3] or breathing effects[4]; those composed of bio-compatible building blocks (bio-MOFs)[5,6,7]; iso-reticular MOFs family (IRMOFs)[8] containing ligands of different lengths that allow the modulation of pores and exhibit exceptional adsorption capabilities. The unique properties exhibited by these materials in many fields account for their great potential in biotechnology and sensor devices fabrication.[9] Currently, given that several thousand MOF structures have already been discovered, control over particle size, morphology, porosity and shaping seems to be crucial for the final implementation of these materials.[10] For this purpose, "bottom-up" and "top-down" methodologies have been developed to try reducing particle size.

Among the coordination networks, those considered as layered structures (2D-CN) are crystalline materials exhibiting anisotropic bonds, due to that there are strong covalent interactions within a plane, while weaker forces are involved in the third dimension, defining the resulting 3D crystal packing. As in the case of other lamellar materials, taking advantage of this anisotropic nature has been an attractive approach to overcome the challenge of splitting bulk materials into atomic layers.[11,12] The huge scientific interest in graphene has led to a wide variety of techniques to produce and process nanolayers that, having nanometric width and mesoscopic lateral size, could be considered as cuasi-2D objects. The capability of producing nanolayers of qualified materials, opens the possibility of thin films fabrication.

Furthermore, CNs can exhibit different responses to the chemical environment, which allow them to exhibit different transduction mechanisms[13] that become suitable for sensing applications.[14]

Particularly, we are interested in taking advantage of the luminescence properties of rare earth elements-based CNs (REE-CNs)[15] for physical[16] or chemical sensing[17].

As it is well known, trivalent lanthanide ions (Ln^{3+}) exhibit low absorption coefficients, due to that the *f-f* transitions are prohibited by the Laporte-parity selection rule. In this regard, vibronic mechanisms can relax this rule and activate absorption. The resulting photoluminescence (PL), even being sharp and having high colour purity, is frequently low in

[a] Instituto de Investigaciones en Tecnología Química (INTEQUI), Área de Química General e Inorgánica "Dr. G. F. Puelles", Facultad de Química, Bioquímica y Farmacia, Universidad Nacional de San Luis, Chacabuco y Pedernera, 5700 San Luis, Argentina.
[b] L3 - Luminescent Lanthanide Lab, Ghent University, Department of Inorganic and Physical Chemistry, Krijgslaan 281, Building S3, 9000 Gent, Belgium.
[c] Instituto de Física Aplicada, Universidad Nacional de San Luis CONICET, Ejército de los Andes 950, 5700 San Luis, Argentina.
[d] Department of New Architectures in Material Chemistry, Institute of Material Science of Madrid, ICMM-CSIC, Sor Juana Inés de la Cruz, 3, Cantoblanco, 28049 Madrid, Spain.
* Corresponding author. E-mail: mcbernin@unsl.edu.ar
Electronic Supplementary Information (ESI) available: crystallographic data (cif), XRPD Refinements, SEM-EDS data, Thermal Analysis, Top-Down procedure and Photoluminescence properties. DOI: 10.1039/x0xx00000x

intensity and needs to be assisted by ligand energy transfer (ET)[18], or even by aromatic guests into porous frameworks.[19] This sensitization pathway is known as "antenna effect" and has been evidenced by us in a Tb-CN when using phenyl-succinate ligand (psa) as linker.[15] However, PL studies of other members of the Ln-psa series (with Ln = Nd, Pr, Sm, Eu, Eu-Gd and Eu-Tb) showed lanthanide-centred luminescence, indicating the importance of obtaining a proper energy gap between the resonant level of the Ln ions and the triplet state of the ligand to exhibit the aforementioned effect.

In previous works, we have studied luminescent REE-CNs based on succinate derivates[15,16,17b]. By means of in situ hydrolysis of the succinyl-salicylic acid, a 3D CN based on succinate and Ho^{3+} was obtained[20], where the salicylic moiety served as a template for constructing the hybrid framework, acting as a guest aromatic species. Continuing with our studies, we have now combined the aliphatic succinate ligand with the aromatic salicylate, and explored the synthesis conditions to obtain a mixed-ligand CN. A novel layered structure with formula [REE(Salicylate)(Succinate)$_{0.5}$(H_2O)] was obtained, where REE = Ho^{3+} or Y^{3+}. The Y^{3+} framework was also doped and co-doped with Tb^{3+} and/or Eu^{3+} ions in order to design novel luminescent materials. Single-crystal X-ray diffraction data and Rietveld refinement of powder X-ray diffraction data were used for the crystallographic characterization, and all bulk phases were studied by thermal analysis, scanning electron microscopy and Fourier-Transform infrared spectroscopy. Liquid exfoliation (LE) by ultrasound, analyzing frequency, power and time as variables, was implemented as "top-down" approach to reduce particle size, tending to optimize the delamination process. Scanning electron microscopy and atomic force microscopy were used to characterize the resulting solid samples. Solid state photoluminescence (SSPL) studies, including excitation/emission spectra and lifetime decays, were performed at room temperature (RT) and in the 10-310 K range, both for bulk samples as well as for colloidal suspensions. Measurements based on the Y^{3+} compound at 70 K were performed to calculate the energy level of the triplet state of the salicylate linker at the solid state. Sensing properties based on the PL behaviors in the presence of different solvents were also studied.

2. Experimental

2.1 Synthesis of [REE(Salicylate)(Succinate)$_{0.5}$(H_2O)] with REE = Ho^{3+} (1) or Y^{3+} (2)

Compounds 1 and 2 were synthesized by mixing 0.5 mmol of succinic acid, 1 mmol of salicylic acid and 1 mmol of each metal ion, respectively; $Ho(NO_3)_3.5H_2O$ (Sigma - Aldrich) was used as Ho^{3+} source, while Y_2O_3 (Sigma - Aldrich) was used for providing Y^{3+} ions. All reactants were dissolved in 20 mL of distilled water under stirring until complete dissolution. The pH was adjusted to 6 for compound 1 and to ≈ 5 for compound 2 by adding trimethylamine. The resulting mixtures were sealed in Parr digestion bombs (internal volume = 43 mL) and heated at 165 °C during 65 h for compound 1, and at 105 °C during 18 h for compound 2. The resulting solids were filtered, washed with distilled water and dried under atmospheric conditions. Regarding compound 1, small plate-like orange single-crystals were selected to perform the single crystal X-ray diffraction (SCXRD) study. Compound 2 was obtained as a fine polycrystalline white powder, and the crystallographic characterization was carried out by PXRD analysis. (Reaction yields: 55-65%).

2.2 Synthesis of [$Y_{(1-x)}(Ln1_{x1},Ln2_{x2})_x$(Salicylate)(Succinate)$_{0.5}$($H_2O$)] with Ln1 = Eu^{3+}; Ln2=Tb^{3+} and x= x1 + x2

The addition of different amounts of Eu and Tb to the reactant solution of compound 2, leads to compounds 3-6. These were synthesized by a similar procedure as for 2, but incorporating 2 mmol% and 5 mmol% of Eu^{3+} to obtain compounds 3 and 4, respectively; while compounds 5 and 6 were obtained by the addition of the same amounts of Tb^{3+}, respectively. The amount of Y^{3+} ions in the reactant mixtures was accordingly decreased to satisfy the general formula. The co-doped phases were obtained by incorporating 2.5 mmol% of Eu^{3+} and 2.5 mmol% of Tb^{3+} (compound 7); 5 mmol% of Eu^{3+} and 2.5 mmol% of Tb^{3+} (compound 8) and 2.5 mmol% of Eu^{3+} and 5 mmol% of Tb^{3+} (compound 9) to each reactant mixture. In all cases, $EuCl_3.6H_2O$ (Sigma - Aldrich) and $TbCl_3.6H_2O$ (Sigma - Aldrich) were used as the lanthanide sources. Water volume and reaction time and temperature were kept fixed as in the synthesis procedure of compound 2. Compounds 3-9 were obtained as white polycrystalline powders, whose isostructural character was analysed by PXRD. (Reaction yields: 40-55%).

2.3 Crystal Structure Determination

Table 1 summarizes the main crystal and refinement data for compound 1. The single-crystal was selected under a polarized optical microscope and glued on a glass fibre for a SCXRD measurement. X-ray intensity data were collected in a Bruker SMART CCD diffractometer equipped with a normal focus, 2.4 kW sealed tube X-ray source (Mo Kα radiation = 0.71073 Å). Data were collected at room temperature over a hemisphere of the reciprocal space by a combination of three sets of exposures. Each exposure of 10 s covered 0.3° in ω. Unit cell dimensions were determined by a least-squares fit of reflections with I >2 σ(I). Data were integrated and scaled using the SAINTplus program.[21] A semi-empirical absorption and scale correction based on equivalent reflection was carried out using SADABS.[22] Space group determination was carried out using XPREP.[23] The structure was solved by direct methods, and refined by least squares minimisation. Multiple specimens were tested to improve the quality of the data. However, the poor diffraction quality of all of them and their twinned nature resulted in relatively high final R values, so that soft restrains on the anisotropic thermal parameters were used during the structural refinement. The hydrogen atoms of the organic ligands were located at their calculated positions. Calculations were carried out with SMART software (for data collection and data reduction) and SHELXTL[24] and OLEX[25] for refinement. The crystallographic information file of compound

1 is deposited at the CCDC (number 1571680) and is also available in the Electronic Supporting Information (ESI).

2.4 X-Ray Powder Diffraction Data (XRPD)

X-ray powder diagrams of all compounds were obtained with a Rigaku D-MAX-IIIC diffractometer using Cu-Kα radiation (Ni filter), and NaCl and quartz as external calibration standards. All diagrams were collected between 3° and 50° in the 2θ range, with a step size of 0.02°. To confirm the obtained crystal structure, the Le Bail method was performed using the FullProf Suite software package[26] to refine the cell and peak profile parameters.

2.5 Fourier Transform Infrared Spectroscopy (FTIR)

FTIR spectra were recorded with a Nicolet Protégé 460 spectrometer in the 4000–225 cm^{-1} range with 32 scans, using the KBr pellet technique and a spectral resolution of 4 cm^{-1}.

2.6 Thermal Analysis

Thermogravimetric (TG) curves and differential scanning calorimetry (DSC) measurements were recorded with a Shimadzu TGA-50H thermal analyser apparatus and a Shimadzu DSC-60 apparatus under flowing air at 50 mL·min^{-1}, at a heating rate of 10 °C·min^{-1}. The TG curves were recorded between RT and 900 °C. The DSC analysis involved two measurements performed as follows: the first one consisted of a heating step from RT to 300 °C and cooling back to RT, then, the sample was removed from the oven and exposed to air for one hour. Afterwards, a second heating step was carried out up to 300 °C, with the same heating rate.

2.7 Photophysical studies

2.7.1 Solid-State Photoluminescence (SSPL) measurements

The steady state and time resolved luminescence measurements were performed on an Edinburgh Instruments FLSP920 spectrometer setup, using a 450 W xenon lamp as the steady state excitation source and a 60 W pulsed xenon lamp as the time resolved excitation source, operating at a pulse frequency of 100 Hz. The emission was detected by a Hamamatsu R928P PMT photomultiplier. Excitation spectra were corrected for the xenon lamp emission profile, whereas the emission spectra were corrected for the detector response curve. All measurements were carried out at a step size of 0.1 nm. Time-resolved measurements were performed using a Continuum® Surelite I laser (450 mJ @1064 nm), operating at a repetition rate of 10 Hz and using the third harmonic (355 nm) as the excitation source. In order to quantify the colour emission, Commission Internationale de l'Eclairage (CIE) (x,y) colour coordinates were calculated using the MATLAB® program employing the emission spectra as input baseline corrected files. The triplet state of the ligand of compound 2 was determined at 70 K, exciting the sample at 320 nm.

Temperature-dependent measurements for compounds 6 and 7 were controlled using an ARS closed cycle cryostat in the 10 – 320 K range (simultaneous measurements were taken every 50 K).

Table 1. Crystal data, structure determination and refinement summary for compound **1**.

Empirical formula	$C_9H_6HoO_6$
Formula mass [g]	375.07
Crystal system	Monoclinic
Space group	$P2_1/c$
a [Å]	21.127(6)
b [Å]	6.0937(16)
c [Å]	7.625(2)
α [°]	90.0
β [°]	92.280(4)
γ [°]	90.0
V [Å^3]	980.9(5)
Z	4
$\rho_{calc.}$[g cm^{-3}]	2.554
T[K]	296.15
Absorption coefficient [mm^{-1}]	8.076
Crystal size [mm]	0.04 x 0.04 x 0.02
T_{min}/T_{max}	0.3609 / 0.5633
h	(-24,24)
k	(-7,7)
l	(-8,8)
Reflections collected/unique [I >2σ(*I*)]	5844 / 1648
Absorption correction	multi-scan
Refined parameters	147
Goodness-of-fit on F^2	1.109
Refinement method	Least Squares
λ [Å]	0.71073
Final R indices [I >2σ(*I*)]	R_1 = 0.0947, wR_2 = 0.2031
Final R indices (all)	R_1 = 0.1573, wR_2 = 0.2452

2.7.2 Chemical sensing studies

The sensing performance of compound 6 was investigated by exposing the exfoliated particles to different organic solvents. The material was prepared as follow: 1 mg of solid was exfoliated by ultrasonication during 60 minutes in 7 mL of absolute ethanol. Then, the suspensions were heated overnight at 70 °C to ensure ethanol evaporation, obtaining the namely 6' material. After that, this material was put directly in contact with 7 mL of each solvent (resulting density of 0.14 mg.mL^{-1}) and sonicated for 15 minutes to ensure the solid dispersion in each medium. The PL spectra of each 6'/solvent suspension were obtained by exciting the samples at 320 nm. The tested solvents (of analytical grade) were toluene, n-hexane, methanol, ethanol, N,N-dimethylformamide and acetone.

View Article Online
DOI: 10.1039/C7TC04006C

2.8 Liquid Exfoliation (LE) experiments

As top-down approach, ultrasonication experiments were performed using 1 mg of compound 6 in 7 mL of absolute ethanol. This mixture was placed in a glass test tube with screw cap and then placed in the ultrasound (ICSA). For procedure details, see ESI.

2.9 Scanning Electron Microscopy (SEM) – Energy Dispersive Spectroscopy (EDS)

SEM was used to study the morphology and particle sizes of the bulk samples as well as those resulting from the LE and SAS experiments. The solid samples and colloidal ethanolic suspensions were placed on the sample holder containing a graphite tape and then covered with a thin Au layer by sputtering. A LEO1450VP microscope provided with an EDS/EDAX probe for microanalysis (LABMEM – UNSL) was used.

2.10 Atomic Force Microscopy (AFM)

The measurements were acquired using a Digital Instruments Multimode AFM with a Nanoscope III controller. The micrographs were acquired in tapping mode with all parameters, including set-point, scan rate and feedback gains adjusted to optimize image quality and minimize the force between the probe and sample. Prior to these measurements, the colloidal suspensions were centrifuged at 4000 rpm for 5 minutes to separate the non-exfoliated solid residues from the supernatant, exhibiting "Tyndall effect". Then, the resulting samples were dispersed by drop casting onto glass flat substrates (0.6 mm x 0.6 mm dimensions) to perform this AFM characterization.

3. Results and Discussion

3.1 Crystal Structure Description.

Compound 1 was studied by SCXRD, being the one selected for the crystallographic description. The isostructural character of the remaining compounds was verified by PXRD refinements (see next section). According to this crystallographic study, compound 1, with formula [Ho(Salicylate)(Succinate)$_{0.5}$(H_2O)], belongs to the monoclinic $P2_1/c$ space group. A summary of the conditions for data collection and structure refinement is given in Table 1. The asymmetric unit is composed by one Ho^{3+} ion, a completely deprotonated salicylate anion, half of a succinate anion and a coordinated water molecule. The lanthanide ion is surrounded by eight oxygen atoms, four of them coming from three salicylate anions, three from two succinate anions, and the last one from the water molecule. The resulting coordination polyhedron (Primary Building Unit, PBU) exhibits triangulated dodecahedron geometry (see Figure 1).

The centrosymmetric succinate linker coordinates as chelate-bridge through its two carboxylate groups. The salicylate anion is tetra-connected since the carboxylate group coordinates two Ln ions as a bidentate-bridge, and the oxygen atom, located in the *ortho* position of the ring, links two metallic ions by a bridge mode (see Figure 1-c). As a result, the polyhedra are condensed by sharing edges, forming one-dimensional chains that run parallel to the [0 0 1] direction and determine the secondary building units (SBUs). The carboxylate groups belonging to the salicylate anion connect the chains in the [0 1 0] direction, while in the ab plane, the SBUs are linked by a zig-zag arrangement of succinate anions (see Figure 2).

This compound can be classified as a 2D coordination network[24] with infinite organic-inorganic layers displayed in the bc plane and packed in the [1 0 0] direction through several "edge-type" C-H···π interactions of 3.29-2.97 Å in distance, which is determined between salicylate anions of adjacent layers (see Figure 2).

Moreover, T-type π-π interactions are also identified inside each layer, reinforcing the self-assembly of building blocks in the [0 0 1] direction.[27]

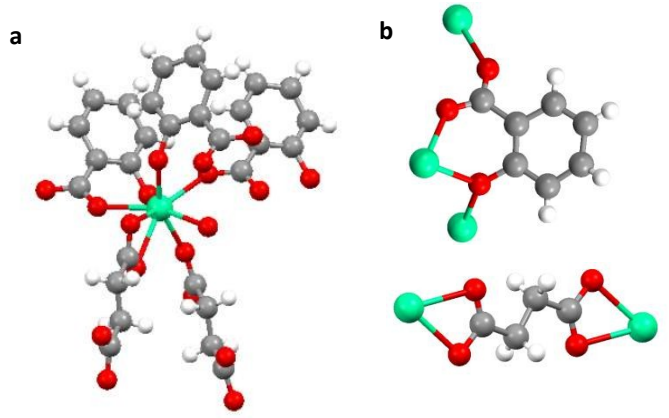

Figure 1. (a) coordination sphere of Ho^{3+} and (b) coordination modes of salicylate and succinate linkers. Colour atoms: grey: carbon, red: oxygen, green: holmium, white: hydrogen.

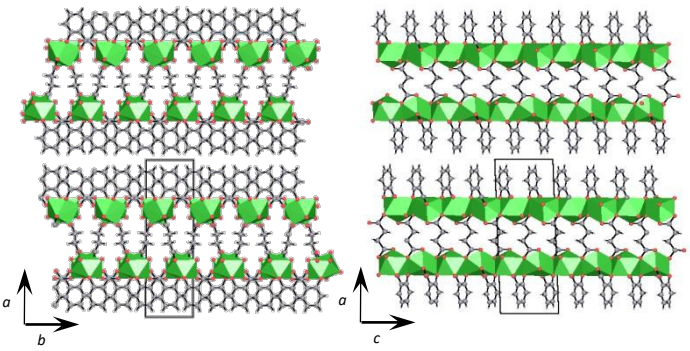

Figure 2. Projections of the structure along the *c* (left) and *b* (right) axis; a unit cell is displayed in each perspective.

According to the IUPAC recommendations,[1,2] analysis of the accessible voids can be performed in order to examine if the structure contains free void volume, and thus being suitable to be called a MOF. To this purpose, the Platon Voids module[28] was used to perform the Solvent Accessible Volume calculation, considering a probe sphere of 1.2 Å in radius. The analysis gave a value of 18.1 $Å^3$, consistent with only 1.8 % of the cell volume. For that reason, this CN should not be classified as a MOF.

3.2 PXRD and Rietveld Refinements

View Article Online
DOI: 10.1039/C7TC04006G

Considering the crystalline model obtained by SCXRD on compound 1, the isostructural character of the remaining compounds was verified by means of PXRD data. Figure 3 shows the comparison between the patterns of the as-synthesized compounds 1-9 and the one simulated from 1, using Mercury 3.3 software.[29] As can be seen, compounds 2, 3, 5, 6 and 7 were obtained as pure phases since no additional peaks are observed in their diagrams. The presence of impurities in the diagrams of compounds 4 and 9 are marked with an asterisk (*). These secondary concomitant phases were also evidenced by SEM, DSC and FTIR characterizations and will be discussed below.

Rietveld refinement on the respective powder diagrams of pure compounds were performed (see Figure S1). Cell and peak profile parameters, as well as those of the background, peak asymmetry, and zero-shift, were considered for the refinements. The resulting agreement indexes are shown in Table S1.

3.3 Solid state characterization

Different solid state techniques were applied to fully characterize the synthesized compounds. According to the SEM analysis, the predominant primary morphology of compounds 2-9 can be described as hexagonal plate-like crystals, while for compound 1 the particles are prismatic (see Figure 4). In all cases, a secondary morphology of spheroidal "rose-like" aggregates is observed. The appearance of some particles with different crystal morphology is evident in compounds 4, 8 and 9, which according to the PXRD data (Figure 3), exhibit a different crystalline phase as impurity. EDS spectra were obtained for all analysed samples in order to determine the chemical composition of the crystals as a semi-quantitative analysis. The calculated amounts (in mmol) of Y, Eu and Tb in the doped and co-doped samples (see Table S2) were used to propose the chemical composition of each compound. by considering the general formula $[Y_{(1-x)}(Ln1_{x1}, Ln2_{x2})_x(Salicylate)(Succinate)_{0.5}(H_2O)]$ with Ln1 = Eu^{3+}, Ln2= Tb^{3+} and $x= x_1 + x_2$.

Thermogravimetric analysis (TGA) was performed to support the proposed chemical formulae and to evaluate the thermal stability of each compound (see Figure S2). According to the calculated and theoretical mass decays (Δm%, see Table S2), the presence (compounds 4, 8 and 9), or absence (compounds 1-3 and 5-7) of impurities was verified through the corresponding degree of agreement between Δm% values.

DSC was performed for all samples in the temperature range of RT-300 °C (see Figure S3) and the thermal behaviours are suitable to be understood in terms of the thermogravimetric variations; the presence of impurities is also evidenced by this technique. For more details see ESI. The corresponding FTIR spectra of all compounds are displayed in Figures S4-S7; the interpretation was made taking into account related bibliography[30] and considering the internal vibrations of methylene, carboxylate and phenoxy groups, aromatic rings, and water molecules. The corresponding assignment is shown in Table S3.

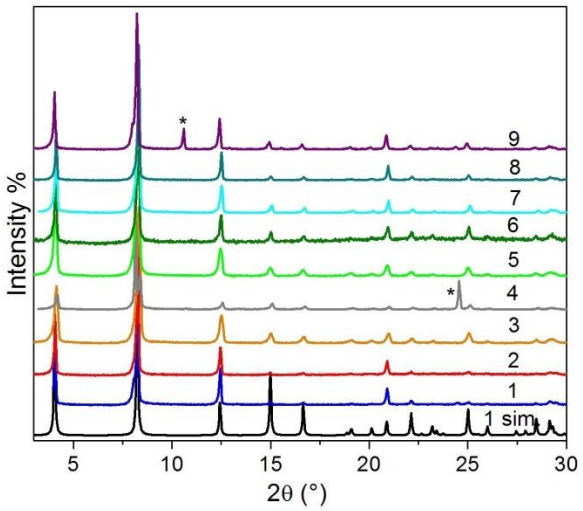

Figure 3. PRXD patterns of the as-synthesized compounds in comparison with the simulated pattern of 1.

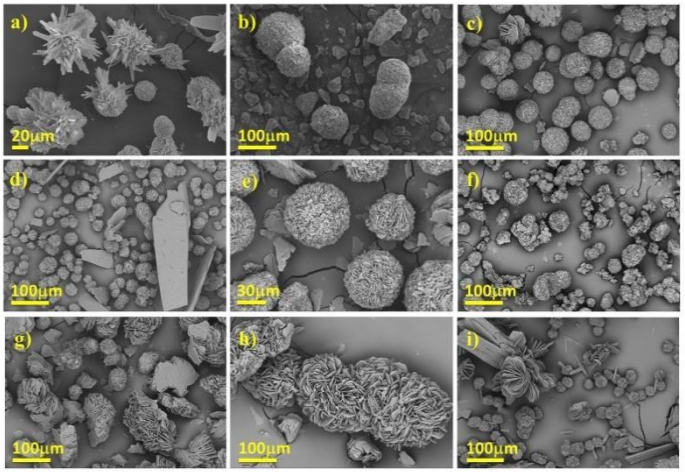

Figure 4. SEM Micrographies of the as-synthesised samples of compounds 1-9 (a-i).

The presence of impurities in compounds 4 and 9 was also evidenced through this characterization technique.

3.4 Ultrasonication treatment

Liquid exfoliation is one of the most common top-down strategies to produce nanolayers of 2D crystalline compounds.[31] Through this procedure, temperatures around 5000 K, pressures of ca. 1000 atm and heating - cooling rates up to ~ 1000 Ks^{-1} can be reached in local spots.[10] In particular, this approach was exploited in CNs materials to obtain nano-objects[32], although a set of nanoparticles of polydispersed width and size is often obtained. The adequate control of the operating conditions may improve the top-down strategy, producing stable colloidal suspensions and tending to avoid the re-aggregation of layers.

For those reasons, a screening of ultrasound frequency, power and exposure time was performed in this work in order to achieve the best conditions to adequately exfoliate the bulk sample of compound 6. This compound was selected because

it exhibits the most brilliant light emission under UV lamp illumination, likely being a promising luminescent material. To select the solvent, preliminary tests (data not shown) were carried out using protic, aprotic and non-polar solvents, among which ethanol resulted to be the most adequate one to perform a deeper study. Two ultrasound frequencies were employed, 40 kHz and 60 kHz. Delamination was observed after 15 minutes at 40 kHz, while no evidence of exfoliation was observed at 60 kHz. A significant amount of colloidal suspension appeared inside the test tubes within 15 minutes at 99 and 165 W, while 30 minutes were necessary with the lowest power value. The resulting suspensions were analysed by SEM (see Figure 5). For the lowest power value, the strong degradation of the laminar particles seems to be evident after 60 minutes (Figure S8). For intermediate and higher power values, the solid particles obtained at the lowest exposure time maintain some crystal features such as edges and angles, and residues of the initial "rose-like" aggregates remain partially degraded. When increasing exposure time, cavitation causes a rapid degradation on the first delaminated particles, leading to a heterogeneous solid residue, with a marked dispersion of sizes and shapes at the highest power setting (Figures S9 and S10). The crystalline nature of the exfoliated solid was verified by PXRD; the structure remains unaltered and the delamination seems not to affect the crystallite size (see Fig. S11).

To complete the characterization of the particles obtained at 30 min and 66 W, AFM studies were performed (see Figure 6).

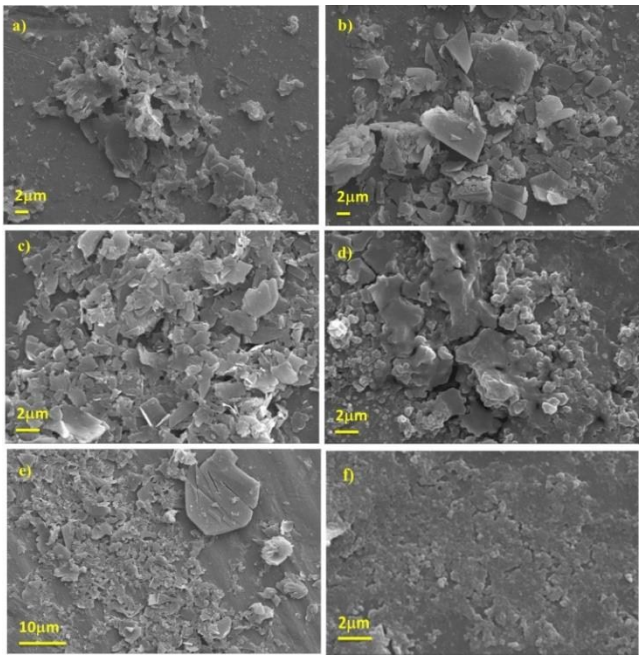

Figure 5. Left column: SEM images obtained at 30 minutes of ultrasound with 66 W (a), 99 W (c) and 165 W (e); Right column: SEM images obtained at 60 minutes of ultrasound with 66 W (b), 99 W (d) and 165 W (f).

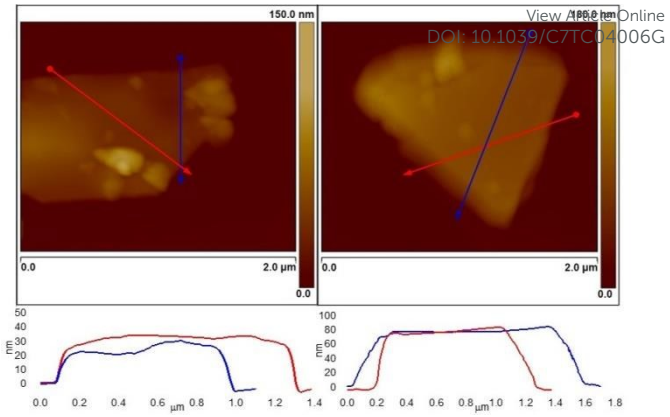

Figure 6. Top: AFM 2D height images of two nanolayers obtained by sonication during 30 minutes with ultrasound weave of 40 kHz and 66 W. Bottom: height profiles of each particle (colour lines correspond to the traces marked in the upper figures).

Prior to dropping the colloidal suspension, a centrifugation step was made in order to separate the heavier particles that could remain not delaminated, as evidenced by SEM (see Figure S9-b). AFM images indicate the presence of exfoliated particles with irregular aspect; exhibiting lateral dimensions of a few microns with heights in the order of tens of nm.

3.5 Solid State Photoluminescence (SSPL) studies

Among rare earth coordination networks and MOFs, those containing Eu^{3+} or Tb^{3+} ions are the most studied as luminescent materials due to their strong sharp emission in the visible region, usually accompanied by high quantum yields and lifetimes. Compounds based on Eu^{3+} are the target of much investigation, not only due to their red-orange light emission, but also because, from a fundamental point of view, it has non-degenerate ground ($^7F_0$) and main emissive ($^5D_0$) states. Compounds containing the strong green emitter Tb^{3+} are also further investigated, since according to its electronic configuration, high- and low-spin states can be generated depending on the coordinated ligands.[33] Moreover, a rational doping of Eu^{3+}/Tb^{3+} ions into diverse inorganic matrices can produce materials with unique spectroscopic properties, where MMCT commonly takes place[16].

In order to avoid the concentration quenching of the lanthanide luminescence, an inactive optic matrix of Y^{3+} ions containing different amounts of dopant contents of Eu^{3+}, Tb^{3+} and a mixture of both, was designed by us in order to obtain the novel 2D luminescent CN. Coordination compounds containing Ho^{3+} can present luminescence at visible (640 nm) and NIR (around 990 nm) regions; however the quantum yields are lower than 0.1%, being more challenging the design of emitting materials based in this lanthanide ion. In the current study, excitation and emission spectra as well as life time decay of compound 1 were obtained (see ESI, Figure S12). A weak emission centred at 1004 nm corresponding to the $^5F_5 \rightarrow {}^5I_7$ transition is observed. The time decay obtained by a single-exponential fitting was of 3.95 ms,

3.5.1 Photophysical properties: Ligand centred transitions

Excitation and emission spectra of compound 2 at RT and 70 K were obtained to characterize the photophysical properties of the salicylate linker. The excitation spectrum obtained at RT was recorded in the 200-350 nm range, monitoring the emission at 410 nm. As can be seen in Figure 7, the broad excitation band has a maximum at 317 nm. and the emission spectrum recorded at RT presents a main broad band centred at 391 nm (25575 cm^{-1}) and an additional weak band at 463 nm (21598 cm^{-1}), which are assigned to the deactivation from the $^1S^*$ to the S_0 state of the salicylate anion. The lowest vibrational basal state is involved in the first emissive transition, while the second lowest one is involved in the second emissive transition.

The emission of compound 2 starts in the UV spectral region and extends up to the visible zone, giving a purplish blue fluorescence (CIE x,y: 0.156,0.020), previously documented for sodium salicylate and salicylic acid.[34] When the sample is cooled at 70 K, the strongest band of the emission spectrum splits into two; one centred at 377 nm (26596 cm^{-1}) and the other at 425 nm (23529 cm^{-1}). These bands may be assigned to the deactivation processes from the $^1S^*$ and $^3T^*$ excited states, respectively. This procedure was previously applied to determine the energy of the excited $^3T^*$ state in Gd^{3+} and Lu^{3+} compounds[35], and is valuable to understand the sensitization mechanisms that can be operative for LMCT.

3.5.2 Photophysical properties of Eu- and Tb- doped compounds

The excitation spectra of compounds 3 and 4 were monitored at the typical wavelength of Eu^{3+} emission, i.e. λ = 611 nm, while those containing Tb^{3+} (5 and 6) were monitored at λ = 541 nm. For compounds 7-9, since the major contribution to the luminescence was due to transitions within the 4*f* shell of the Tb^{3+} ion, the monitoring wavelength was the same.

As discussed in section 3.3, the presence of a secondary phase as impurity was evidenced in compound 4.

For this reason, differences in the excitation and emission spectra of this compound, in comparison with those of compound 3, could be expected. Here, we will discuss in major detail only the luminescence results of the pure samples. As can be seen in Figure 8, the excitation spectrum of compound 3, recorded by excitation through the $^1S^*$ of the ligand, exhibits a wide band similar to that described for compound 2, corresponding to $S_0 \rightarrow {}^1S^*$ transitions of the salicylate anion[36]. It is also observed the appearance of a band at 393 nm, which can be ascribed to the $^5L_6 \leftarrow {}^7F_0$ transition of Eu^{3+} ions.

For compound 4, the components of the spectrum seem to be the same as 3, although some differences in the relative intensities are observed.

The emission spectra of compounds 3 and 4 exhibit a strong band centred at 468 (21367 cm^{-1}) and 471 nm (21231 cm^{-1}), respectively. These results reflect a poor sensitization of the Eu^{3+} ion by the salicylate ligand and can be explained in terms

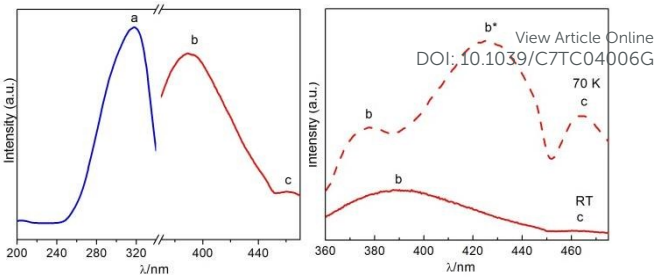

Figure 7. Left: Excitation (blue) and emission (red) spectra of compound 2 at RT. Right: Emission spectra at RT (solid line) and 70 K (dash line).

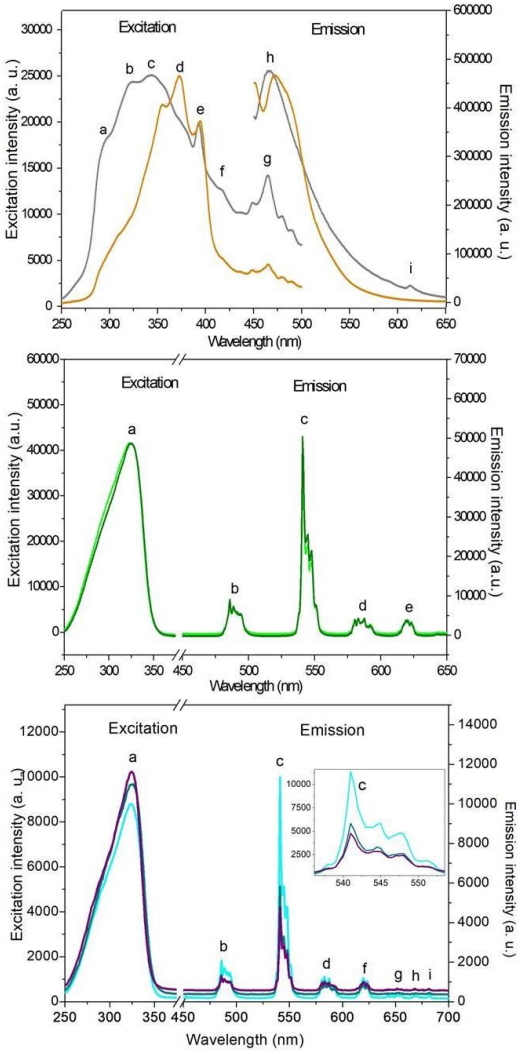

Figure 8. Excitation and emission spectra of compounds 3, 4 (top); 5, 6 (middle); 7-9 (bottom). Colour code of compound spectra: 3, grey; 4, orange; 5, green; 6, olive; 7, cyan; 8, dark cyan; 9, purple. The inset in the bottom image shows a zoom of the hypersensitive transition $^5D_4 \rightarrow {}^7F_5$ of Tb^{3+} ion.

of the energy difference between the excited $^1S^*$ state (26596 cm^{-1}) and the $^3T^*$ state (23529 cm^{-1}), therefore a difference of 3062 cm^{-1}, which is quite lower than the suggested (5000 cm^{-1}) as the optimum energy difference that maximizes the $^1S^* \rightarrow {}^3T^*$ intersystem crossing.[35] Even when this is not the only operative mechanism for the sensitization of Ln^{3+} ions, it is the most frequent one; but since the ΔE ($^3T^*$ - $^5D_0$) is 4500 cm^{-1}, an

effective energy transfer from the excited states of the linker to the emissive state $^5D_0$ of the Eu^{3+} ion is hardly plausible.

Studies on Eu-doped compounds have allowed to propose that the antenna effect is maximum when the $^3T^*$ 0-phonon transition lies at 2500-3500 cm^{-1} above the lanthanide excited state.[37]

The excitation spectra of compounds 5 and 6 (Figure 8) show a strong absorption band in the 250-350 nm range, that is also due to the $S_0 \rightarrow {}^1S^*$ transition of the salicylate anion. No evidence of Tb^{3+} electronic transitions lines is observed in these spectra; however, the emission spectra exhibit the typical bands corresponding to Tb^{3+} luminescence due to the $^5D_4 \rightarrow {}^7F_J$ (J=6-2) transitions.

An efficient ET process from the linker to Tb^{3+} ions is observed when compounds 5 and 6 are exited at the salicylate wavelength. This fact suggests that small amounts of Tb^{3+} could quench the fluorescence of salicylate anion by a LMCT mechanism, known as *antenna effect*.

According to our measurements for compound 2, the energy of the $^3T^*$ state of the salicylate is only 2529 cm^{-1} above the emissive $^5D_4$ state of the Tb^{3+} ion. This result indicates an effective sensitization of this ion in both, compound 5 and 6, yielding a strong green SSPL at RT with CIE x,y chromaticities of 0.317,0.602 (see Figure 9 with the CIE diagram). Even though the ET from the $^3T^*$ state to the emissive state of the Tb^{3+} ions seems to be the most probable mechanism, sensitization via direct migration from the $^1S^*$ of the ligand has also been documented for Eu^{3+} and Tb^{3+} complexes[18a] and cannot be totally discarded for the present compounds (see Scheme 2).

The luminescence decay profiles of the $^5D_4 \rightarrow {}^7F_5$ emission of compounds 5 and 6 were measured (see Figure S13). The data was fitted with single exponential equations, from which the lifetime can be calculated as τ_{obs} = 1.066 ms (5) and 1.077 ms (6). As can be seen, not only by the slight intensity increase of the spectra but also in the τ_{obs} values, the increment in the Tb^{3+} content from 4.4 mmol% in compound 5 to 6.5 mmol% in compound 6, does not reach the minimum limit amount to exhibit concentration quenching effects, and thus compound 6 shows a better performance as green light emitter.

Regarding the SSPL properties of compounds 7-9 (see Figure 8), it is interesting to remark that, even though Tb^{3+} could sensitize the Eu^{3+} emission, no signals derived from this ion appear in the spectra of the co-doped compounds; only the transitions $^5D_4 \rightarrow {}^7F_J$ (J=6-0) of the Tb^{3+} ion can be observed. Comparing the intensity of the emission spectra, and focusing in the $^5D_4 \rightarrow {}^7F_5$ hypersensitive signal of Tb^{3+}, it is possible to observe that a combination of two sources of quenching are operative in compounds 7-9, since the highest intensity is obtained for compound 7 while a decrease is observed not only when the Eu^{3+} content is increased (compound 8) but also when the Tb^{3+} content is increased (compound 9).

Scheme 2. Jablonski diagram showing the ET paths between salicylate and Ln^{3+} ions in compounds 2, 3-7.

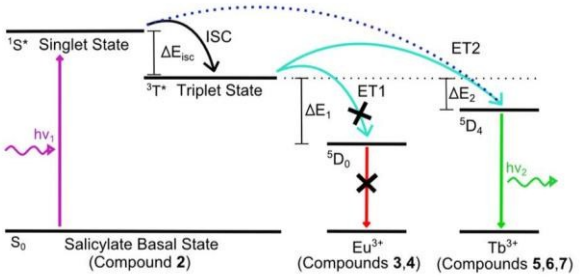

This fact suggests that in compound 9, the Tb^{3+} self-quenching is operative along with a quenching effect originated by Eu^{3+}.

3.5.3 Influence of the top-down processing on the luminescence properties

Since compound 6 shows the best performance as green light emitter, and in order to determine the incidence of the particle size reduction on the SSPL performance, emission spectra and decay-time were measured for a sample of an ethanolic suspension of exfoliated particles and for the same sample after ethanol evaporation (see Figure S14). The spectra show that the typical Tb^{3+}-centred luminescence bands and their relative intensities are similar.

Focusing on the most intense peak corresponding to the hypersensitive transition, it is possible to observe a lower intensity for the ethanolic suspension sample, which exhibits 39% of the bulk sample intensity.

A similar behaviour was also identified in our previous study on PL properties of ethanolic suspensions containing exfoliated Eu-psa 2D frameworks particles[15a], where the role of O-H groups in the solvent medium as oscillator-quenchers of the Ln luminescence, contributes to decrease the emission intensity.

To confirm this fact, the spectrum of the dried compound 6 was obtained after solvent evaporation, where the intensity increased again, keeping 60% of the initial value (bulk sample). As can be deduced by these experiments, a loss of 40% of the emission intensity is caused by the stress provoked by the cavitation process during the LE treatment. A number of studies dealing with optimizing power, depth position of the ultrasound source, type of cavitation and the nature of the liquid medium, are devoted to investigate nanosheet formation of graphene oxide or layered transition metal dichalcogenide.[38] For these types of materials, highly reactive radicals and by-products formed by the sonolysis of organic solvent molecules can unexpectedly influence the dispersion of nanomaterials in organic solvents. For this reason, minimizing surface defects formation is essential to maintain the electronic properties in optimum performance. However, as far as we know, no analogous studies for CNs have been reported.

View Article Online
DOI: 10.1039/C7TC04006E

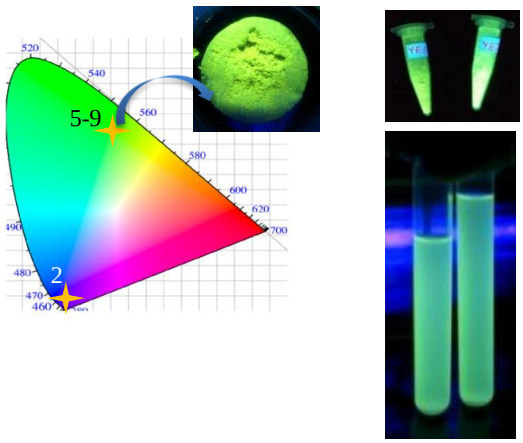

Figure 9. CIE diagram showing the chromaticity coordinates x,y for compounds 2 and 5-9. The picture shows the naked-eye photoluminescence of compound 6 under UV illumination.

From our experiments, we can deduce that the loss of 40% of the emission intensity in the exfoliated dried sample is related to surface defects, which can be punctual or extended. The former ones are associated with vacancies, being the most frequent due to the linker; the later ones are derived from imperfections of the crystal structure in one or two dimensions. Considering the physical treatment achieved via ultrasonication[39], a combination of both types of defects is expected. However, since the antenna effect was confirmed as operative to sensitize the Tb^{3+} luminescence, ligand vacancies could justify the decrease in the resultant emission intensity.

The incidence of the top-down procedure is also evident in the calculated decay-time (τ_{obs}); being 1.078 ms for the bulk sample, 1.102 ms for the ethanolic suspension and 1.127 ms for the exfoliated dried sample. Since the τ_{obs} can be estimated as:

$$\tau_{obs} = 1/(krad + \sum knrad) \qquad \text{(Eq. 1)}$$

the slight elongation in the time decay can be due to a decrease in the sum of the non-radiative and radiative velocity constants. Since the decrease in particle size introduces a higher surface/volume ratio, the number of emitting ions on the surface of the exfoliated solid should be higher than in the bulk sample, thus contributing to the decrease in the self-quenching occurring when emissive ions are adjacent. Finally, LE seems to incorporate surface defects that decrease the number of emitted photons (lower spectrum intensity), but since the number of survival emissive ions in the particle surface is higher, the concentration quenching is reduced, giving rise to a slightly longer τ_{obs} after exfoliation and solvent evaporation.

3.5.4 Temperature sensing studies

Thermal sensing and mapping in an accurate and non-invasive manner are important features for the development of devices with direct impact on nano-science[40]. Specific requirements for temperature monitoring in harsh and/or hardly accessible environments has prompted the development of several non-contact methods for temperature measurements, exploiting a change of optical properties, i.e. emission intensity, refractive index, wavelength shift, luminescence decay time, etc., with temperature. [41]

In this context, REE-CN and REE-MOFs have attracted particular interest, mainly for the possibility of tuning the colour and spectroscopic behaviour by controlling the lanthanide doping[42], this being a key factor for thermo-sensor design. Recently, several ratiometric thermometers based on lanthanoid metal–organic frameworks (MOFs) have been reported containing a mixture of lanthanide ions, mainly Eu^{3+} and Tb^{3+}.[43] Extending the sensing temperature range to below 50 K is of great value for both cryogenic research and industrial applications, e.g. energy and space exploration.[44]

The SSPL activity from cryogenic to RT was studied for compounds 6 and 7 in terms of excitation and emission spectra, and through the corresponding fluorescence intensity ratio (FIR). The excitation spectra at seven different temperatures were recorded in the λ = 250–350 nm range, and the corresponding emission spectra were monitored at λ = 541 nm (18484 cm^{-1}, Figure 10-top). No evidence of 4*f* transitions of the Ln^{3+} ions was observed in the excitation spectra, neither for compound 6 nor 7. Focusing on compound 6, the excitation intensity corresponding to the $S_0 \rightarrow {}^1S^*$ transition of the salicylate linker, rapidly decreases in the 10-110 K range, then increases at 160 K, and finally remains practically constant up to 310 K.

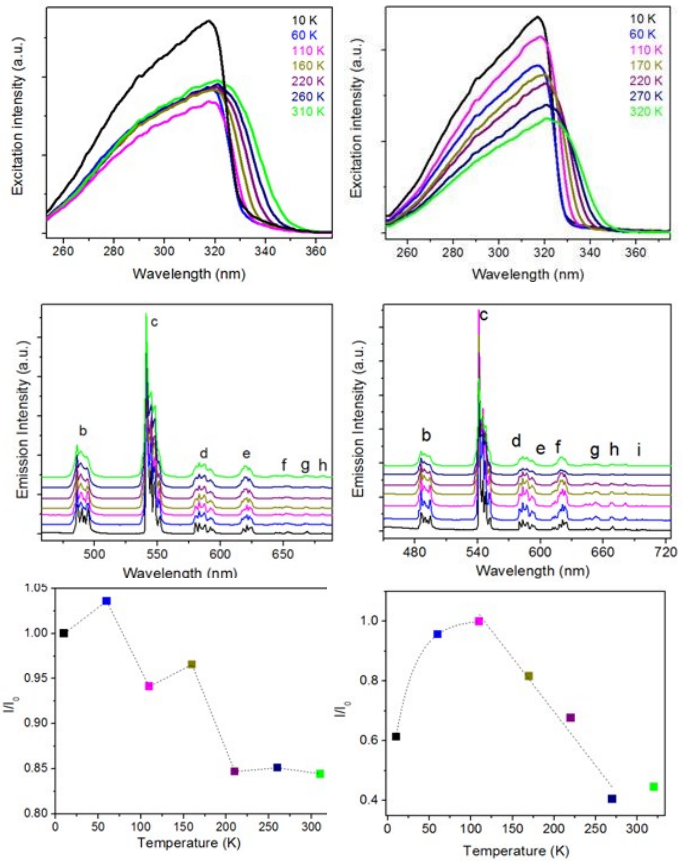

Figure 10. Excitation (top) and emission (middle) spectra of compound 6 (left) and 7 (right) obtained in the 10-310 K temperature range. Calculated FIR of 6 and 7 (bottom).

The behaviour of compound 7 is clearly different since the excitation intensity decreases when the temperature goes from 10 to 60 K, then it suffers a marked increase at 110 K, and finally decreases gradually and continuously up to 320 K.

Upon excitation at λ_{exc} = 320 nm (31250 cm^{-1}) in the 10–320 K temperature range, both compounds show the typical narrow Tb^{3+} emission peaks ($^5D_4 \rightarrow {}^7F_J$, J=6-0; see Figure 10-middle). For compound 7, the $^5D_0 \rightarrow {}^7F_2$ transition from Eu^{3+} ions appears in the 10-220 K range as a weak signal (see Figure 10-middle). At the higher temperature, the compound exhibits only the Tb^{3+} luminescence. According to the analysis of the CIE x,y chromaticity of both compounds along the entire temperature range, the colour coordinates do not present changes (CIE x,y: 0.317,0.601) and only green light emission is appreciated.

However, a complex variation in the intensity of the spectra appears in both compounds when the temperature is increased from 10 K to 310 K (see Figure 10).

FIR considers the ratio between the fluorescence intensity at each temperature (**I**) and the intensity of the Tb^{3+} hypersensitive transition at the lowest temperature ($\mathbf{I_0}$). One important variable for a thermal sensor is the Sensitivity (**S%**), which can be calculated as the slope of the FIR curve vs T[45]:

$$\mathbf{S\% = |\Delta FIR/\Delta T| \cdot 100} \qquad \text{(Eq. 2)}$$

For compound 6, the thermal dependence of the FIR in the range of 10-310 K is characterized by a non-linear and non-exponential decrease corresponding to 15% of the initial value (Figure 10-bottom left). In the case of compound 7, the FIR exhibits a quite striking behaviour since it suffers an exponential increase in the 10-110K range, followed by an almost linear decrease between 110-270 K (Figure 10-bottom right). Therefore, the S% should be calculated in different ways according to the temperature range. For the 10-110 K, where the exponential profile is fitted satisfactorily as I/I0 = -0.593·exp(-T/24.338), the S% is calculated by averaging the slopes of the linear segments of the curve, giving a value of 0.43%·K^{-1}. Above 110 K, the FIR linear trend can be fitted as I/I0 = 1.4196-0.00361·T and the calculated S% value is 0.361% K^{-1}. A similar S value (0.366%·K^{-1}) was found using $[Eu_{0.8}Tb_{1.2}(psa)_3(H_2O)]$[15], whose FIR vs T curve exhibited an exponential decay in the 13.5-313.5 K temperature range. The SSPL properties of compounds 6 and 7 demonstrate the influence of the Eu-Tb co-doping system, since even though the dominating luminescence is only due to Tb^{3+}, the incorporation of Eu^{3+} may generate defects, reducing the Ln site symmetry. The presence of Eu^{3+} induces changes in the electronic band structure of the solid, which leads to multiple excited bands with several and varied overlapping energies. This fact could introduce novel splitting in the Stark sub-levels, which in turn conduct to a different Tb intensity emission as a function of temperature.

3.5.5 Chemical-sensing experiments

CNs have been widely employed as platforms to sense organic solvents[46], VOCs (volatile organic compounds)[17a,47], water[48] and inorganic ions.[49] Moreover, the use of these compounds in the detection of hazardous substances, such as explosive-like molecules[50], is of current interest.

The chemosensing performance of the exfoliated compound 6 (6´) was investigated by measuring the PL of this solid in the presence of three protic (water, methanol and ethanol) and four aprotic (DMF, chloroform, n-hexane and acetone) solvents (see Figure 11).

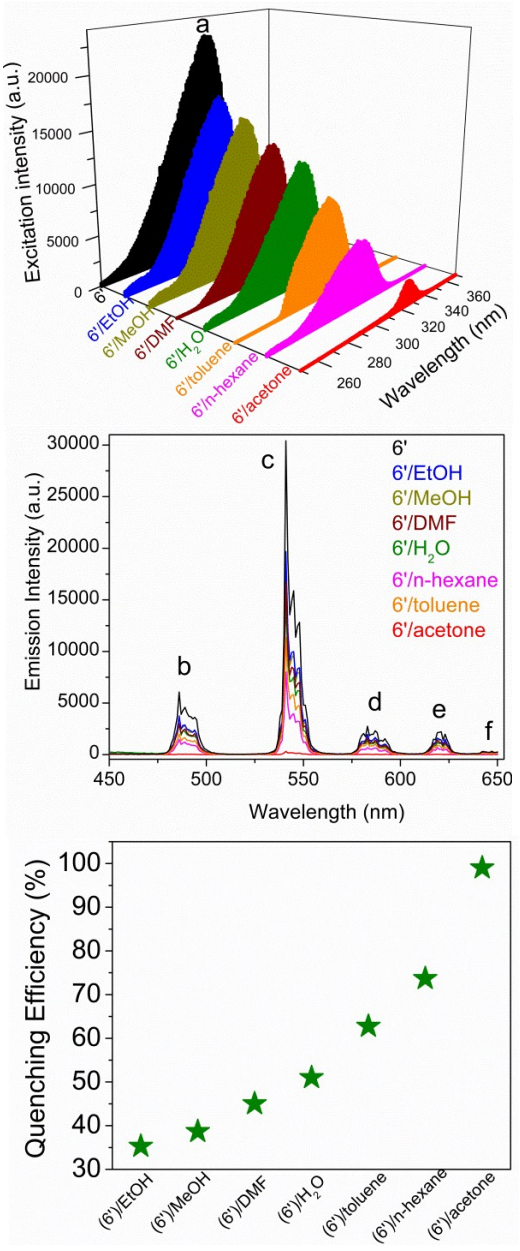

Figure 11. Excitation (top) and emission (middle) spectra, and QE% (bottom) of compound 6' in the presence of different solvents.

The PL performance of compound 6´ in absence of solvents was considered for comparison purposes, and the emission intensities and lifetimes were taken into account as sensing parameters. The excitation band centred at 320 nm (31250 cm^{-1}) suffered an important decrease when the compound was in

a suspension of toluene, n-hexane and acetone; being maximum for acetone, reaching a signal reduction of 90% compared with compound 6'.

A similar trend was identified in the emission spectra, since the quenching of the hypersensitive transition in the presence of these solvents is remarkable.

The Quenching Efficiency (QE) can be defined as:

$$QE\% = (I_0 - I)/I_0 \cdot 100 \quad \text{(Eq. 3)}$$

where I_0 and I represent the emission intensity values in the absence and presence of solvent, respectively.

Based on these results, acetone represents an efficient quencher for the luminescence of compound 6', exhibiting a QE of 98%, being the highest value for the set of aprotic solvents. The high selectivity for acetone detection can be explained in terms of the absorption *competition quenching mechanism*[51], since a full overlap between acetone absorption and the excitation spectra of compound 6´ is evidenced. This fact leads to a competition of absorption of the light source between the analyte and the CN, which causes the luminescence quenching of compound 6´. This mechanism was also demonstrated as operative in the acetone mediated luminescence quenching of a Tb-doped cadmium-MOF.[52]

Among the protic solvents, as expected, water represents the most efficient quencher with a QE of 51%.

The analysis of the influence of the solvents on the PL properties of compound 6' was also evaluated in terms of lifetimes values (See Figure S15 and Table S6). The decrease in τ_{obs} (see Table S6) matches well the increase of the QE% values, where compound 6' exhibits a prominent quenching effect in solvents with terminal C=O and C-H groups (toluene, DMF, n-hexane and acetone) in comparison with the solvents containing O-H groups (water, ethanol and methanol).

Conclusions

A new set of isostructural crystalline layered REE-CNs with a general formula [REE(Salicylate)(Succinate)$_{0.5}$(H_2O)] (REE = Ho (1) or Y(2)), were hydrothermally synthesized and fully characterized. A controlled lanthanide doping on (2) was carried out by the addition of Eu^{3+}, Tb^{3+} and Eu^{3+}-Tb^{3+}.

Liquid exfoliation was explored as a top-down technique allowing the delamination of the bulk phase of a Tb-doped compound. Crystal particles of lateral dimensions of a few microns and heights in the order of tens of nm were obtained, achieving a width reduction of about 90-95%.

The SSPL of the samples 2-9 were studied in terms of excitation/emission spectra, lifetime values and quantification of light emission by calculating the CIE x,y chromaticities.

The energy transfer pathways involved in the sensitization mechanism of Tb^{3+} and Eu^{3+} ions were studied by the determination of the $^1S^*$ and $^3T^*$ energy levels through SSPL spectra of compound 2. An antenna effect was operative in the case of Tb-containing compounds, while in the Eu-doped ones the effective sensitization by the linker was discarded.

Thermal-sensor performances of compounds 6 and 7 were evaluated in the 10–310 K range as a function of the emission intensity of the hypersensitive $^5D_4 \rightarrow {}^7F_5$ transition. For compound 7, the yielding sensitivities were of 0.43% $\cdot$ K^{-1} in the 10-110 K range, where an exponential FIR increase is observed, while 0.361 % $\cdot$ K^{-1} is obtained in the 110-270 K range, where a linear FIR decrease is apparent.

According with the high performance of compound 6 as green emitter, the chemical sensing tests were evaluated in the presence of protic and aprotic solvents, finding that the presence of acetone produces an efficient QE of ~98%, which suggests compound 6 as a promising candidate for the development of sensors of carbonyl-containing compounds.

The highly optically active Tb-doped CN obtained here, could generate a platform for the preparation of efficient luminescent green emitter devices.

Acknowledgements

This work was supported by the Consejo Nacional de Investigaciones Científicas y Técnicas (PIP- CONICET 11220150100820CO), and PROICO 2-2016 (UNSL-INTEQUI). R.V.D. thanks the Hercules Foundation (project AUGE/09/024 "Advanced Luminescence Setup") for funding. A.A.G. acknowledges a CONICET fellowship, A.M.K. acknowledges Ghent University's Special Research Fund (BOF) for a Postdoctoral Mandate (project BOF15/PDO/091). G.E.N., O.J.F. and M.C.B. are members of CIC-CONICET.

References

1 S. R. Batten, N. R. Champness, X. M. Chen, J. Garcia-Martinez, S. Kitagawa, L. Öhrström, M. O'Keeffe, M. Paik Suh and J. Reedijk, *Pure Appl. Chem*., Vol. 85, No. 8, pp. 1715–1724, 2013.

2 S. R. Batten, N. R. Champness, X.-M. Chen, J. Garcia-Martinez, S. Kitagawa, L. Öhrström, M. O'Keeffe, M. Paik Suh and J. Reedijk, *CrystEngComm*, 2012, 14, 3001.

3 D. Fairen-Jimenez, S. A. Moggach, M. T. Wharmby, P. A. Wright, S. Parsons, T. Duren, J. Am. Chem. Soc. 2011, 133, 8900-8902.

4 a) C. Serre, S. Bourrelly, A. Vimont, N. A. Ramsahye, G. Maurin, P. L. Llewellyn, M. Daturi, Y. Filinchuk, O. Leynaud, P. Barnes, G. Férey, Adv. Mater. 2007, 19, 2246-2251; b) A. Boutin, S. Couck, F.-X.Coudert, P. Serra-Crespo, J. Gascon, F. Kapteijn, A. H. Fuchs, J. F. M. Denayer, Microp. Mesop.Mater.140 (2011) 108-113; c) A. Boutin, D. Bousquet, A. U. Ortiz, F.-X.Coudert, A. H. Fuchs, A. Ballandras, G. Weber, I. Bezverkhyy, J.-P.Bellat, G. Ortiz, G. Chaplais, J.-L.Paillaud, C. Marichal, H. Nouali, J. Patarin, J. Phys. Chem. C. 2013, 117, 8180-8188.

5 a) J. An, S. J. Geib, N. L. Rosi, J. Am. Chem. Soc. 2009, 131, 8376-8377; b) J. An, O. K. Farha, J. T. Hupp, E. Pohl, J. I. Yeh, N. L. Rosi, Nat. Commun. 2012, 3:604. 1-6.

6 a) P. Horcajada, T. Chalati, C. Serre, B. Gillet, C. Sebrie, T. Baati, J. F. Eubank, D. Heurtaux, P. Clayette, C. Kreuz, J. S. Chang, Y. K. Hwang, V. Marsaud, P. N. Bories, L. Cynober, S. Gil, G. Férey, P. Couvreur and R. Gref, *Nat. Mat.* 9, 172–178 (2010); b) V. Agostoni, T. Chalati, P. Horcajada, H. Willaime, R. Anand, N. Semiramoth, T. Baati, S. Hall, G. Maurin, H. Chacun, K. Bouchemal, C. Martineau, F. Taulelle, P. Couvreur,

C. Rogez-Kreuz, P. Clayette, S. Monti, C. Serre, and R. Gref, *Adv Healthcare Mater*. 2013; 2 (12):1630-7; c) C. Tamames-Tabar, D. Cunha, E. Imbuluzqueta, F. Ragon, C. Serre, M. J. Blanco-Prieto, P. Horcajada, J. Mater. Chem. B, 2014, 2, 262-271.

7 J. Rabone, Y.-F. Yue, S. Y. Chong, K. C. Stylianou, J. Bacsa, D. Bradshaw, G. R. Darling, N. G. Berry, Y. Z. Khimyak, A. Y. Ganin, P. Wiper, J. B. Claridge, M. J. Rosseinsky *Science* **2010** 329 (5995):1053-7.

8 a) M. Eddaoudi, J. Kim, N. L. Rosi, D. T. Vodak, J. Wachter, M. O'Keeffe, O. M. Yaghi, Science, 2002, 295, 469-472; b) H. Deng, S. Grunder, K. E. Cordova, C. Valente, H. Furukawa, M. Hmadeh, F. Gándara, A. C. Whalley, Z. Liu, S. Asahina, H. Kazumori, M. O'Keeffe, O. Terasaki, J. F. Stoddart, O. M. Yaghi, Science, 2012, 336,1018-1023; c) S. Chavan, J. G. Vitillio, D. Gianolio, O. Zavorotynska, B. Civalleri, S. Jakobsen, M. H. Nilsen, L. Valezano, C. Lamberti, K. P. Lillerud, S. Bordiga, Phys. Chem. Chem. Phys., 2012, 14, 1614-1626; d) M. J. Katz, Z. J. Brown, Y. J. Colón, P. W. Siu, K. A. Sheidt, R. Q. Snurr, J. T. Hupp, O. K. Farha, Chem. Commun., 2013, 49, 9449-9451; e) C. Janiak and J. K. Vieth, *New J. Chem*., 2010, 34, 2366–2388.

9 R. Ricco, C. Pfeiffer, K. Sumida, C. J. Sumby, P. Falcaro, S. Furukawa, N. R. Champness, C. J. Doonan, *CrystEngComm*, **2016**,18, 6532-6542.

10 B. Seoane, S. Castellanos, A. Dikhtiarenko, F. Kapteijn, J. Gascon, *Coord. Chem.Rev*. 307 (2016) 147–187.

11 K. S. Novoselov, D. Jiang, F. Schedin, T. J. Booth, V. V. Khotkevich, S. V. Morozov and A. K. Geim, *PNAS*, 2005, Vol. 102, No. 30, 10451–10453.

12 K. Kouroupis-Agalou, A. Liscio, E. Treossi, L. Ortolani, V. Morandi, N. M. Pugnodfgh, V. Palermo, *Nanoscale*, 2014, 6, 5926–5933.

13 (a) M. Meilikhov, S. Furukawa, K. Hirai, R. A. Fischer and S. Kitagawa,Angew. Chem., Int. Ed., 2013, 52, 341; (b) G. Lu and J. T. Hupp,J. Am. Chem. Soc., 2010, 132, 783.; (c) A. L. Robinson, V. Stavila, T. R. Zeitler, M. I. White, S. M. Thornberg, J. A. Greathouse and M. D. Allendorf, Anal. Chem., 2012, 84, 7043; (d) M.Ohba, K. Yonedaand, S. Kitagawa, *CrystEngComm*., 2010,12, 159; (e) Y. J. Cui, Y. F. Yue, G. D. Qian and B. L. Chen, Chem. Rev., 2012,112, 1126; (f) Y. Cui, B. Chen and G. Qian, Coord. Chem. Rev., 2014,273, 76; (g) M. D. Allendorf, R. J. T. Houk, L. Andruszkiewicz, A. A. Talin, J. Pikarsky, A. Choudhury, K. A. Galland P. J. Hesketh, J. Am. Chem. Soc., 2008, 130, 14404.

14 I. Stassen, N. Burtch, A. Talin, P. Falcaro, M. Allendorf, R. Ameloot Chem. Soc. Rev., 2017,46, 3185-3241.

15 a) G. E. Gomez, M. C. Bernini, E. V. Brusau, G. E. Narda, D. Vega, A. M. Kaczmarek, R. Van Deun and M. Nazzarro, Dalton Trans., 2015, 44, 3417. b) G. E. Gomez, M. C. Bernini, E. V. Brusau, G. E. Narda, W. A. Massad, A. Labrador, Cryst. Growth Des.2013, 13, 5249–5260.

16 G. E. Gomez, A. M. Kaczmarek, R. V. Deun, E. V. Brusau, G. E. Narda, D. Vega, M. Iglesias, E. Gutierrez-Puebla and M. Á. Monge, *Eur. J. Inorg. Chem*., 2016, 1577–1588.

17 a) R. F. D'Vries, G. E. Gomez, D. F. Lionello, M. C. Fuertes, G. J. A. A. Soler-Illia, J. Ellena, RSC Adv., 2016, 6, 110171-110181. b) G. E. Gomez, E. V. Brusau, A. M. Kaczmarek, C. Mellot-Draznieks, J. Sacanell, G. Rousse, R. Van Deun, C. Sanchez, G. E. Narda, G. J. A. A. Soler Illia, Eur. J. Inorg. Chem., **2017**, 2321-2331.

18 a) Y. Cui, Y. Yue, G. Qian and B. Chen, *Chem. Rev.* 2012, 112, 1126–1162. b) M. Allendorf, V. Stavila, CrystEngComm, 2015,17, 229-246.

19 D. T. de Lill, A. de Bettencourt-Dias, C. L. Cahill, *Inorg. Chem.* **2007**, *46*, 3960–3965.

20 M. C. Bernini, N. Snejko, E. Gutierrez-Puebla, E. V. Brusau, G. E. Narda, M. A. Monge, *Inorg. Chem.*, Vol. 50, p. 13, 2011, 5958-5968.

21 SAINT Data Collection and Procedure Software for the SMART System, Siemens Analytical X-ray Instruments Inc., Madison, WI, USA,1995.

22 SHELXTL, v. 5.0, Siemens Analytical X-ray Instruments Inc., Madison, WI, 1995.

23 SMART, v. 5.04 and SHELXTL, v. 5.1, Bruker-Siemens Analytical X-ray Instrument, Inc., Madison, WI, USA, 1998.

24 P. T. Anastas, J. C. Warner, Green Chemistry: Theory and Practice, Oxford University Press, New York, 1998.

25 Dolomanov, O.V., Bourhis, L.J., Gildea, R.J, Howard, J.A.K. & Puschmann, H. (2009), J. Appl. Cryst. 42, 339-341.

26 FULLPROF: Rodriguez-Carvajal, J.Physica B1993, 192,55−69.

27 C. Janiak J. Chem. Soc., Dalton Trans., 2000, 3885–3896.

28 Spek, A. L. Acta Crystallogr. A 1990, 46, C34.

29 C. F. Macrae, I. J. Bruno, J. A. Chisholm, P. R. Edgington, P. McCabe, E. Pidcock, L. Rodriguez-Monge, R. Taylor, J. van de Streek and P. A. Wood, J. Appl. Cryst., 2008, 41, 466-470.

30 a) M. C. Bernini, E. V. Brusau, G. E. Narda, G. E. Echeverría, C. G. Pozzi, G. Punte, C. W. Lehmann, Eur. J. Inorg. Chem. 5 (**2007**) 684. b) M. C. Bernini, J. C. Garro, E. V. Brusau, G. E. Narda, E. L. Varetti, J. Mol. Struct. 888 (**2008**) 113.

31 Z. Y. Xia, S. Pezzini, E. Treossi, G. Giambastiani, F. Corticelli, V. Morandi, A. Zanelli, V. Bellani and V. Palermo, *Adv. Funct. Mater*., 2013, 23, 4684–4693.

32 a) Y. Peng, Y. Li, Y. Ban, H. Jin, W. Jiao, X. Liu, W. Yang, *Science*, Vol. 346, Issue 6215, pp. 1356-1359. b) J.- C. Tan, P. J. Saines, E. G. Bithell and A. K. Cheetham, *ACS Nano*, 2012, 6/1, 615.

33 J.- C. G. Bünzli, *Coord. Chem. Rev.* 293–294 (2015) 19–47.

34 a) G. Stein, M. Tomkiewicz, *Trans. Faraday Soc*. 1971, 67, 1009-1015. b) A. Saltzman, *J. Biol. Chem.* 1948, 174, 399-404.

35 S. V. Eliseeva and J. C. G. Bünzli, *Chem. Soc. Rev*., 2010, 39, 189–227.

36 S. Maheshwari, A. Chowdhury, N. Sathyamurthy, H. Mishra, H. B. Tripathi, M. Panda, J. Chandrasekhar *J. Phys. Chem. A* 1999**,** *103,* 6257-6262.

37 R. Rodríguez-Cortiñas, F. Avecilla, C. Platas-Iglesias, D. Imbert, J.- C. G. Bünzli, A. de Blas and T. Rodríguez-Blas, *InorganicChemistry*, Vol. 41, No. 21, 2002.

38 (a) W. Qiao, S. Yan, X. He, X. Song, Z. Li, X. Zhang, W. Zhong and Y. Du, *RSC Adv*.,**2014**,4, 50981–50987. (b) J. T. Han, J. I. Jang, H. Kim, J. Y. Hwang, H. K. Yoo, J. S. Woo, S. Choi, H. Y. Kim, H. J. Jeong, S. Y. Jeong, K.-J. Baeg, K. Cho and G.-W. Lee, Sci Rep., **2014**; 4:5133.

39 (a) Z. Fang, B. Bueken, D. E. De Vos, and R. A. Fischer, *Angew.Chem.Int. Ed.* 2015, 54, 7234 –7254. (b) David S. Sholl and Ryan P. Lively, *J. Phys. Chem. Lett.* **2015**, 6, 3437−3444.

40 C. D. S. Brites, P. P. Lima, N. J. O. Silva, A. Millán, V. S. Amaral, F. Palacio, L. D. Carlos, *Nanoscale* **2012**, *4*, 4799-4829.

41 V. B. Mykhaylyk, A. Wagner, H. Kraus *J. Synchrotron Rad.* (2017). 24, 636–645.

42 (a)F. Le Natur, G. Calvez, C. Daiguebonne, O. Guillou, K. Bernot, J. Ledoux, L. Le Pollès, C. Roiland, *Inorg. Chem.*, **2013**, *52(11)*, 6720-6730. (b) X. Fan, S. Freslon, C. Daiguebonne, G. Calvez, L. Le Pollés, K. Bernot, O. Guillou, *J. Mater. Chem. C*, **2014**, *2*, 5510-5525.

43 a) C. D. S. Brites, P. P. Lima, N. J. O. Silva, A. Millan, V. S. Amaral, F. Palacio, L. D. Carlos, *Adv. Mater.* **2010**, *22*, 4499–4504; b) S. Katagiri, K. Manseki, Y. Tsukahara, K. Mitsuo, Y. Wada, *J. AlloysCompd.* **2008**, *453*, L1–L3; c) X. Wang, X. G. Kong, Y. Yu, J. Sun, H. Zhang, *J. Phys. Chem. C* **2007**, *111*, 15119–15124; d) M. A. R. C. Alencar, G. S. Maciel, C. B. de Araujo, A. Patra, *Appl. Phys. Lett.* **2004**, *84*, 4753–4755.

View Article Online
DOI: 10.1039/C7TC04006G

44 X. Liu, S. Akerboom, M. de Jong, I. Mutikainen, S. Tanase, A. Meijerink, E. Bouwman *Inorg. Chem*., **2015**, 54 (23), 11323–11329.
45 X.-D. Wang, O. S. Wolfbeis, R. J. Meier, Chem. Soc. Rev., **2013**, *42*, 7834-7869.
46 B. Chen, Y. Yang, F. Zapata, G. Lin, G. Qian and E. B. Lobkovsky, *Adv. Mater.*, **2007**, 19, 1693-1696.
47 H. Xu, X. Rao, J. Gao, J. Yu, Z. Wang, Z. Dou, Y. Cui, Y. Yang, B. Chen and G. Qian, *Chem. Commun.*, **2012**, 48, 7377-7379.
48 Y. Yu, J.-P. Ma and Y.-B. Dong, *CrystEngComm*, **2012**, 14, 7157-7160.
49 B. Chen, L. Wang, F. Zapata, G. Qian and E. B. Lobkovsky, *J. Am. Chem. Soc.*, **2008**, 130, 6718-6719.
50 S. Pramanik, C. Zheng, X. Zhang, T. J. Emge and J. Li, *J. Am. Chem. Soc.*, **2011**, 133, 4153-4155.
51 L. Guo, X. Zeng, J. Lan, J. Yun, D. Cao, *ChemistrySelect* **2017**, 2, 1041 – 1047.
52. H. Weng, B. Yan, *Sensors and Actuators B* **2016**, 228, 702–708.

View Article Online
DOI: 10.1039/C7TC04006G

Graphical abstract

A new family of luminescent 2D coordination networks: energy pathways for sensitization mechanisms and chemical-physical sensing features.